Modeling the effect of voids on solid composite propellant deflagration and mechanics

Caleb Munger, Jenna Stocker, Eric Sandall and Brandon Runnels*

Department of Aerospace Engineering, Iowa State University, Ames, IA 50011, USA

ARTICLE INFO

Keywords:
Solid composite propellants, Solid rocket motors, Propellant regression, Voids, Arbitrary geometry, Phase-field modeling

ABSTRACT

Voids can form within solid composite propellants (SCPs) during various stages of production and use, altering burn characteristics and subsurface mechanical response. This can be hazardous because the actual burn rate may be different from predicted values (altering the thrust profile and reducing controllability) and because the stresses may exceed nominal values (leading to damage or fracture). This work presents a stabilized phase-field formulation for simulating SCP deflagration in void-containing mesostructures. The formulation extends a previously developed full-feedback regression model by introducing a temperature-cutoff mobility that suppresses subcritical interface motion, preventing nonreacting void surfaces from evolving due to curvature-driven artifacts while preserving high-temperature regression behavior. The stabilized model is applied to ammonium perchlorate (AP) / hydroxyl-terminated polybutadiene (HTPB) mesostructures with AP sizes between 2.5 µm and 15.0 µm at 1 MPa and 7 MPa gauge pressures, with and without voids inside AP particles. The simulations predict regions of maximum temperature, fluctuations in instantaneous burn rate, and stress fields induced by nonuniform thermal expansion and pressure loading during regression. Predicted regression rates agree with experimental data within 28% error for all geometries at 1 MPa, while high-pressure results capture relevant trends but indicate the need for additional gas-phase or radiative heat-transfer physics. These results provide a physics-based framework for investigating how void morphology alters SCP regression and subsurface mechanical response.

1. Introduction

Solid rocket motors (SRMs) have been used for many decades and are a common means of delivering commercial and scientific payloads to orbit [1]. A notable example is the Artemis II rocket system, which used two SRMs as boosters to help send a crewed mission around the moon. Solid rocket motor operation involves the uncontrolled deflagration of solid composite propellants (SCPs) [2], with combustion products typically accelerated through a converging-diverging nozzle to generate thrust. SCPs are heterogeneous mixtures of fuel, such as hydroxyl-terminated polybutadiene (HTPB), and oxidizer, such as ammonium perchlorate (AP). Other additives are often included, such as carbon [3] to increase burn rate, or aluminum [4, 5] to increase the energy density.

The mesoscale structure and morphology of the SCP plays a key role in achieving reliable, predictable burn behavior. Defects, such as voids, may significantly alter SCP performance and reliability. Void defects can be introduced at many stages within a propellant's life cycle. First, voids can be introduced in the manufacturing process, as mixing and casting [6] with volatile contaminants can cause voids to form from gaseous products after the mixture has been poured [7]. Additive manufacturing of rocket motors can also lead to void formation between layers [8, 9]. Second, voids can form during storage, due to de-wetting, especially if strained, aged, or exposed to moisture [10]. When operating in extraterrestrial environments, impacts from micrometer sized debris can erode surfaces and send shock waves through the vessel, causing void formation [11]. Finally, voids can form during the deflagration process due to the evolving mechanical and thermal loading. In all cases, the presence of voids can impact the performance of SCPs by altering burn rates, in some cases increasing rates by over 50% [12], affecting rocket trajectory and possibly compromising mission objectives [13], or causing catastrophic motor failure in extreme cases [14]. Predicting and understanding their effects is essential for improving safety and ensuring success of missions using SRMs for propulsion.

To understand and predict SCP burn behavior, both experimental measurements and computational modeling techniques are required. Experimental studies provide important validation data on regression rates [15] and material failure [16]. However, such experiments can be expensive, hazardous, and time consuming to perform [17]. Further, it is not currently possible to ascertain experimentally the subsurface mechanical state induced by deflagration, making it difficult to determine the risk of mechanical failure induced by voids in the SCP. The extensive amount of testing required to identify and verify the safety and performance of each new propellant formulation makes implementing new technologies (additional additives, additive manufacturing, mesoscale grain design, etc.) in new SRMs difficult and costly. To enable the use of novel propellant formulations and manufacturing methods, the ability to rapidly iterate and provide detailed physics-based understanding of SCP behaviors is needed.

*Corresponding author
brunnels@iastate.edu (B. Runnels)
ORCID(s): 0009-0009-0051-0522 (C. Munger); 0009-0006-3651-8882 (E. Sandall); 0000-0003-3043-5227 (B. Runnels)

Modeling enables rapid design iteration, providing detailed understanding of SCP performance without the costs or hazards of experiments. Computational modeling provides *in situ* information about mesostructure burn surface evolution, heat flux, and deformation at small length and time scales, helping to inform and predict experimental results. A number of models have been proposed that predict both the solid and gas phase of an SCP, but are limited to a singular valued surface function of the geometry [18–20]. Other methods have included chemistry models [21–23] in the gaseous phase to resolve the thermochemistry near the burn surface in AP/HTPB propellants without voids. These explicit mappings even allow for the calculation of mechanical stress and strain inside the binder [24–26]. However experimental imaging of SCPs has shown that the burn surface is complex, and at times not singular valued [27–31], so alternate methods to coordinate mapping are needed to track the burn surface. Level-set methods have been employed for surface tracking [32, 33], but these methods are generally non-conservative and require expensive reinitialization to maintain the level-set's signed-distance-function property for numerical accuracy [34–36]. Diffuse boundary methods have also been employed to implicitly track complex boundaries [37, 38], allowing non-singular valued surfaces to be studied. At the larger scale, models for motors made of SCPs with voids have been developed and are used for motor-sized geometries [39–41], but mesoscale-level regression rate changes are not captured. Machine learning approaches have also been employed for a variety of applications in the design of energetic materials, such as predicting detonation velocity and pressure [42, 43], and have been shown to capture burn rate data [44], but models can be limited by the availability of training data and do not provide thermal analysis. Other models study the ignition of propellants, and have been bench marked to experimental data, but do not model the continued deflagration of the propellant [45]. Despite the numerous existing modeling approaches, numerical efforts for capturing the full thermal and mechanical response induced by voids remain limited.

This work addresses that gap by extending a previously developed full-feedback phase-field model for SCP burn surface evolution to void-containing mesostructures. The central modeling advance is a temperature-cutoff mobility law that suppresses interface motion below the onset of sustained AP/HTPB deflagration. This prevents void and solid-gas interfaces from evolving under subcritical, curvature-driven artifacts while preserving the high-temperature regression behavior calibrated in prior work. With this stabilization, the model can simulate arbitrary void morphologies, image-derived mesostructures, and surrogate porous or hollow AP particles. A validated elastic solver and Neo-Hookean model are then coupled to the stabilized burn model to compute stress and strain in the solid phase under thermal expansion and constant pressure loading [46].

The remainder of the work is structured in the following way: Section 2 develops the updated full-feedback phase-field model and strong form finite kinematics solver for this work. Section 3 demonstrates the regression of a generated mesostructure with highly irregular geometries to demonstrate the model's capacity for arbitrary morphologies and prediction of the mechanical response in an experimental mesostructure, before presenting comparison to experimental results for AP/HTPB propellants with and without voids. Results and conclusions are summarized in Section 4.

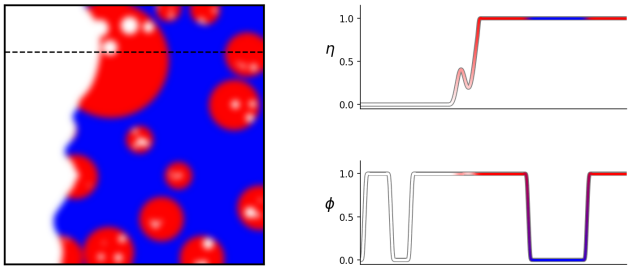

Figure 1: Representative example of phase-field modeling for SCP regression. The red areas $\phi = 1$ are AP, and the blue $\phi = 0$ is HTPB. The white regions are empty regions $\eta = 0$ and are used to model voids inside the domain.

2. Methods

This section presents an updated and stabilized phase-field model based on the previously developed full-feedback phase-field model and strong form elastic solver. This model was originally developed by Kanagarajan et al. [37]; which was extended to the full-feedback formulation by Meier et al. [38] and integrated with hyperelasticity in Meier and Runnels [46]. Physically motivated extensions to this model are shown to help capture the effects of SCP regression with voids.

2.1. Full-feedback phase-field model

Phase-field methods offer an implicit, diffuse-interface tracking through the use of a a field variable (ex, η) that acts as a smooth, pointwise-valued reaction coordinate (Fig. 1). The phase-field method regularizes the sharp interface problem by diffusing the interface region over a defined interface width (characterized by controllable parameter ϵ) to ensure differentiability everywhere in the domain, including the interfacial region, so that the interface can be implicitly tracked. Phase-field models are predicated on the construction of an appropriate free energy functional that captures the physics of interest and is applied to a field that can have two distinct values (i.e. 0 or 1), indicative of the corresponding species or phases. In the limit as $\epsilon \to 0$, provided the phase field is correctly formulated, the free energy converges (formally, $\Gamma-$converges) to the sharp interface solution, ensuring that the error incurred through the implicit representation of the interface remains bounded and controllable.

The field variable $\eta : \Omega \times \mathbb{R} \to [0, 1]$, where $\Omega \subset \mathbb{R}^n$ is the domain of interest and η is required to be twice differentiable in space, implicitly tracks the state of the material in the continuum region. The material inside the continuum region is either solid ($\eta = 1$), or burned ($\eta = 0$),

and $0 < \eta < 1$ is the diffuse interface. While the gas phase is not explicitly resolved in the present method, a gas model is implemented, effectively providing the boundary conditions needed to evolve the interfacial region. Here, the free energy functional

$$F[\eta] = \int_\Omega \left[\frac{\lambda}{\epsilon} w(\eta) + \frac{1}{2} \epsilon \kappa |\nabla \eta|^2 \right] dx, \tag{1}$$

captures the thermodynamics driving the deflagration of the propellant and, consequently, the movement of condensed phase interface. λ controls the magnitude of the chemical potential, w is the chemical potential, κ is the interface energy, and ϵ is the diffuse thickness of the interface. The evolution of the unburned region is determined by the partial differential equation,

$$\frac{\partial \eta}{\partial t} = -\frac{L}{\epsilon} \frac{\delta F}{\delta \eta} = -\frac{L}{\epsilon} \left[\frac{\lambda}{\epsilon} \frac{\partial w}{\partial \eta} - \epsilon \kappa \Delta \eta \right], \tag{2}$$

where L is the mobility of the interface controlling the interface velocity. The geometry is accurately captured as long as $\epsilon << \ell$, the smallest length scale of interest. When this is not the case (as is sometimes inevitable in the case of corners or material interfaces), negative curvature can cause the Laplacian in Eq. (2) to become large, causing $\partial\eta/\partial t$ to be positive and resulting in an unphysical "healing" behavior of the solid. To prevent this non-physical curvature driven effect, a simple but effective remediation is to clamp $\partial\eta/\partial t$ to zero when $\partial\eta/\partial t > 0$.

The mobility, L, relates the regression rate to the thermodynamic driving force and therefore controls whether a local interface is allowed to move. In previous work, this mobility was prescribed with an Arrhenius rate law,

$$L = A \exp\left(\frac{-E_\mathrm{a}}{R_\mathrm{u} T} \right), \tag{3}$$

where A is the pre-exponential factor, R_u is the universal gas constant, T is temperature, and E_a is activation energy, all of which are dependent on the species indicator field, ϕ, which differentiates between AP and HTPB (Fig. 1).

The Arrhenius form gives a nonzero mobility for any $T > 0$. This is acceptable for an actively burning interface, but it becomes problematic for void-containing mesostructures because cold, nonreacting internal surfaces can still evolve under the curvature terms in Eq. (2). In that case, interface motion is driven by numerical diffuse-interface energetics rather than sustained condensed-phase deflagration. To suppress this subcritical motion, the present work replaces the Arrhenius mobility with a temperature-cutoff mobility. Experimental evidence indicates that below 640 K, AP/HTPB combustion is endothermic [47, 48]. Although AP and HTPB can still thermally decompose below this temperature, the decomposition timescale is much longer than the deflagration timescale considered here [49]; for the present mesoscale regression model, the corresponding interface mobility is therefore taken to be zero. Thus, Eq. (3) is modified to

$$L = \begin{cases} 0, & T < T_\mathrm{cutoff} \\ A \exp\left(\frac{-E_\mathrm{a}}{R_\mathrm{u} T} \right), & T \geq T_\mathrm{cutoff} \end{cases}, \tag{4}$$

where $T_\mathrm{cutoff} = 640\,\mathrm{K}$ in the present work. Above the cutoff, the original Arrhenius kinetics are recovered; below the cutoff, void surfaces and other nonreacting interfaces remain stable until sufficient heating occurs. Related piecewise temperature couplings have also been shown to be effective in resolving complex boundary-driven phenomena in other application domains (e.g. [50–52]).

Since the mobility depends on local temperature, it is necessary to model the subsurface temperature field driven by the heat flux from the gas phase. This temperature evolution in the condensed phase is driven by the heat flux from the gas phase, $\hat{q} = \hat{q}(x, t, \eta, \dot{\eta}, \phi, \ldots)$, determined by the reacting flow field. Because the determination of $\hat{q}$, which requires simulation of the fully-resolved flow field, can be computationally expensive, it is desirable to approximate $\hat{q} \approx \hat{q}(\dot{m}, p, \phi)$, a surrogate model that relates the local heat flux to the local mass flux, pressure, and species composition. This heat flux / mass flux relationship is estimated from Gross and Beckstead [53] which is amenable to piecewise polynomial fitting

$$\hat{q}_\mathrm{AP} = C_1^\mathrm{AP}\, p + C_0^\mathrm{AP} - \frac{\zeta_0}{\zeta}, \tag{5}$$

$$\hat{q}_\mathrm{HTPB} = C_1^\mathrm{HTPB}\, p + C_0^\mathrm{HTPB} - \frac{\zeta_0}{\zeta^{-1}}, \tag{6}$$

$$\hat{q}_D = C_2^\mathrm{D}\, p^2 + C_1^\mathrm{D}\, p + C_0^\mathrm{D} - \frac{1}{2} q_\mathrm{AP} - \frac{1}{2} q_\mathrm{HTPB}, \tag{7}$$

where C are determined by fit to experimental or numerical data. The parameter ζ_0 is a reference length scale for the diffuse interface between AP and HTPB, which allows for the polynomial to be scaled to different diffuse thicknesses without changing the overall heat flux; however, ζ will vary depending on the length scale of the propellant. Larger ζ values smooth out the transition between the AP and HTPB, reducing the maximum temperature and reducing the burn rate. In the present work, different ζ values are used to reflect the differing length scales of the AP particles and the voids in the domain.

Because the regression rate is locally determined by temperature, the heat equation must be solved concurrently in a diffuse boundary setting. Temperature evolution is driven by the flux across the burn surface as described above, but since the boundary is represented implicitly, a diffuse source is used to effect this boundary condition

$$\eta \frac{\partial T}{\partial t} = \frac{1}{\rho\, c_p} \nabla \cdot (\eta\, \kappa\, \nabla T) + |\nabla \eta| \frac{q_0}{\rho\, c_p} \tag{8}$$

where ρ is density and c_p is specific heat of the material. (It was shown in [38] that this is equivalent to the sharp-interface in the $\epsilon \to 0$ limit.) Though mathematically exact, Eq. (8) is degenerate when $\eta = 0$, causing lack of uniqueness and, consequently, numerical instability. To remediate this,

Table 1
Physical parameters for AP/HTPB thermo-mechanical modeling. Cited parameters come from previous literature, others have been tuned to fit the model.

Parameter	Symbol	Combined	AP	HTPB
Activation Energy (K)	E_A		$11 \cdot 10^3$ [19]	$7.5 \cdot 10^3$ [19]
Base Mass Flux (kg/m^2)	$\dot{m}_0$		$1 \cdot 10^3$	$5 \cdot 10^3$
Bulk Modulus (MPa)	κ		15162.134 [54]	1368.519 [54]
Density (kg/m^3)	ρ		$1.95 \cdot 10^3$ [12]	920 [12]
Heat Flux Scaling Factor (W/μm^2)	Q		$10 \cdot 10^6$	0.147
Pre-exponential Factor (m/s)	A		$145 \cdot 10^3$ [20]	14[20]
Reference Pressure (MPa)	P_{ref}	1.1		
q̂ Constant (-)	C_0	$C_0^D = -0.3715 + \frac{\zeta_0}{\zeta}$	$C_0^{AP} = 420 \cdot 10^{-3}$	$C_0^{AP} = 323 \cdot 10^{-3}$
q̂ Pressure Factor (MPa^{-1})	C_1	$C_1^D = 2.01$	$460 \cdot 10^{-3}$	$1114 \cdot 10^{-3}$
q̂ Pressure Square Factor (MPa^{-2})	C_2	$C_2^D = -0.09906$		
Reference Interface Width (μm)	ζ_0	10.0	10.0	10.0
Shear Modulus (MPa)	μ		14191.376 [54]	2.465 [54]
Specific Heat (J/(kg K))	c_p		$1.2979 \cdot 10^3$ [55]	920 [55]
Temperature Cutoff (K)	T_{cutoff}	640 [47, 48]		
Thermal Conductivity (J/(m s K))	k		$418.6 \cdot 10^{-3}$ [55]	$146.3 \cdot 10^{-3}$ [55]
Thermal Expansion Coef. (1/K)	α		$2.217 \cdot 10^{-5}$ [56]	$5.1 \cdot 10^{-6}$ [57]

a stand-in temperature in the burned region is prescribed in order to ensure that the temperature field is well-defined everywhere in the domain (even if it is not actually needed everywhere):

$$T_{\text{total}} = \eta\, T_{\text{solid}} + (1-\eta)\, T_{\text{burned}}, \tag{9}$$

where T_{burned} is the arbitrarily-chosen stand-in for the temperature in the burned region.

2.2. Strong form elasticity

To compute the elastic response during regression, a strong form elastic solver is utilized. Since the timescales of acoustic wave propagation in the solid (order of $\sim 10^3$ m/s [58, 59]) are much faster than the movement of the burn surface (order of $\sim 10^{-2}$ m/s [38, 60]), a quasi-static approximation is used to solve for the elastic response. The diffuse potential energy of the system is,

$$\Pi[\chi] = \int_\Omega \left(\left[\mathrm{W}(\mathbf{F}) - \chi \cdot \mathbf{B} \right] \eta + \chi \cdot \mathbf{T} |\nabla \eta| \right) dV, \tag{10}$$

where W is the elastic free energy functional, $\mathbf{F} = \text{grad}(\chi)$ is the deformation gradient, $\mathbf{B}$ is the body force, and $\mathbf{T}$ is the surface traction over the natural boundary. By minimizing the potential energy from Eq. (10), the Euler-Lagrange equations follow the application of minimum potential energy,

$$\text{Div}\left(\eta \frac{\partial \mathrm{W}}{\partial \mathbf{F}} \right) - \eta\, \mathbf{B} = T |\nabla \eta|, \tag{11}$$

which is the stress-divergence equation for large deformations. In the SCP there are multiple species, to compute the stress response in this solid-solid interface region a linear scaling based on their relative concentrations is,

$$\mathrm{W}(\mathbf{F}) \mapsto \sum_{n=1}^{N} \phi_n(\mathbf{X})\, \mathrm{W}_n(\mathbf{F}), \quad \sum_{n=1}^{N} \phi_n = 1, \tag{12}$$

where the elastic solver can solve for the response in an arbitrary number of species in the domain. A neo-Hookean hyperelastic model is used for the AP/HTPB with energy functional [61, 62],

$$\mathrm{W}(\mathbf{F}) = \frac{\mu}{2} \left(\frac{\text{tr}\mathbf{F}^T\mathbf{F}}{J^{2/3}} - \dim \right) + \frac{\kappa}{2}(J-1)^2, \tag{13}$$

where μ is the shear modulus, κ is the bulk modulus, $\mathbf{F}$ is the deformation gradient tensor, and $J = \det \mathbf{F}$. After solving for the deformation, the strain and stress are found with the Green-Lagrange strain tensor and the Cauchy stess tensor,

$$\mathbf{E} = \frac{1}{2}\left(\mathbf{F}^T\mathbf{F} - \mathbf{I} \right), \quad \sigma = \frac{1}{J}\mathbf{P}\mathbf{F}^T, \tag{14}$$

where $\mathrm{P} = \partial \mathrm{W} / \partial \mathbf{F}$ is the Piola-Kirchhoff stress tensor. This method is used to report the stress and strain of the propellant in the Eulerian frame. As a stand in for the fluid phase, a diffuse constant pressure traction term is applied at the burn surface,

$$\mathbf{T} = \begin{cases} 0, & T < T_{\text{cutoff}} \\ -p\, \nabla \eta, & T \geq T_{\text{cutoff}} \end{cases}, \tag{15}$$

where p is the constant pressure stand in for the fluid phase.

2.3. Implementation

Diffuse boundary methods are notoriously costly due to the increased resolution required at diffuse boundaries, necessitating the use of adaptive mesh refinement (AMR). This work employs a block-structured adaptive mesh refinement (BSAMR), enabling dynamic resolution of regions with steep gradients while minimizing overall computational cost. The full-feedback model used in this work is implemented in Alamo [63], which is built on AMReX, an open source AMR framework that provides BSAMR

[64]. Alamo employs a multiple-inheritance polymorphic integrator framework to abstract numerical time integrations of coupled multiphysics models, enabling the integration of the full-feedback model with elasticity, fluid flow, etc.

Best practice in phase field and diffuse boundary methods is to ensure that at least 5 grid points span the length of the diffuse boundary in order to avoid mesh-dependent anisotropy [65]; however, convergence testing is still essential. The model was tested for convergence with respect to mesh size and timestep (Appendix A), and the 5-element criterion was found to be sufficient to ensure reasonable accuracy without excessive computational cost. As such, all meshes in the present work are constructed to have a minimum of 5 elements through the smallest length scale of interest, though the starting mesh size and AMR level naturally vary depending on the domain and mesosctructure under consideration. The convergence study also determined that the time step has no appreciable impact on the results as long as it is small enough not to violate the CFL[1] condition [66].

Burn rates are estimated during postprocessing by considering the evolution of the isocontour $\eta = 0.5$ over time. The furthest point along the isocontour is selected as the burn front, and a central difference derivative approximation is used to calculate the regression rate, mimicking the experimental tripwire method for determining burn rates [67, 68].

3. Results

This section evaluates the stabilized formulation in increasingly realistic void-containing mesostructures. The first case isolates geometric complexity by forcing regression around a highly curved, non-singular void surface; the second initializes the model from an experimental image; and the final cases compare predicted burn rates with experimental measurements for porous, hollow, and void-free AP particles. After simulating SCP deflagration, VisIt [69] is used to post process temperature, stress, strain, and solid-burned interface contours. Most physical constants used in this study are unchanged from previous work (Table 1). Simulation metadata and animations for Figs. 3 to 5 and 8 are included in supplementary information.

3.1. Nontrivial geometry

The first test is designed to exercise the cutoff mobility in a geometry where curvature-driven artifacts would be most likely to appear. An artificial AP/HTPB mesostructure with a complex void is created and tested. The initial configuration of the AP/HTPB is generated using threshold dynamics, a method of constructing synthetic mesostructures by thresholding random fields [70]. This is done by placing a 4000 by 4000 grid of random values between 0 and 1 and then iteratively smoothing and thresholding to get a grain with diffuse boundaries. The generated grain is 47% AP and 53% HTPB by volume (Fig. 2) and is placed on a 1 mm by 1 mm domain. A spiral-shaped void is added for two reasons. First, the void exposes the condensed phase to inward- and outward-facing surfaces so that regression proceeds in multiple directions throughout the simulation. Second, the burn surface is not single valued, so a coordinate mapping method would require repeated remapping as the interface evolves. To initiate SCP regression, a laser at the center of the domain is simulated by applying a heat flux of $100\,\mathrm{MW/m^2}$ for 1 ms, which matches experimental setups where a high powered laser is shone on an SCP to initiate the exothermic reaction of AP and HTPB [71].

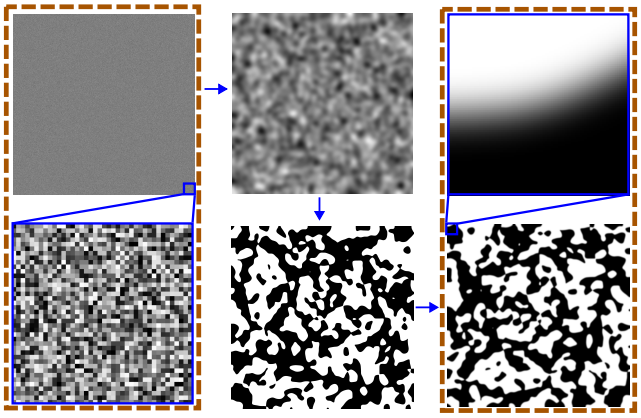

Figure 2: Generation of representative grain for the full-feedback model. From left to right, initial random value placement in a 4000 by 4000 grid, smoothed random placement, thresholded values to make synthetic grain, and smoothed grain for the phase-field model.

The resulting burn follows the spiral pattern of the void, indicating that the internal void surface remains geometrically stable until it is reached by the heated regression front (Fig. 3). Because gas-phase transport and radiation are not explicitly simulated, the condensed-phase interface does not propagate through empty regions; instead, regression proceeds along the solid surfaces exposed by the void. During regression, peak temperature areas reside within HTPB, while the surface moves fastest and releases the most heat in mixed AP/HTPB regions. The higher temperatures observed within the HTPB binder can be attributed to its slower regression rate, which results from a lower pre-exponential factor compared to AP. Although AP exhibits a higher heat flux than HTPB, its faster burn rate promotes heat transfer into the surrounding binder, leading to greater heating of the HTPB relative to the AP itself Fig. 3. As the front moves through the domain, local regression accelerates along exposed spiral edges because these regions have increased solid-gas interfacial area. This behavior is represented through the Laplacian term in Eq. (2): near a void surface, η approaches a local minimum, increasing $\Delta\eta$ and accelerating local interface recession once the cutoff temperature is exceeded. The case therefore demonstrates the intended role of the temperature-cutoff mobility: cold void surfaces remain stable, while heated surfaces regress

[1] The stability condition for reaction-diffusion equations is not, strictly speaking, a CFL condition; however, it is so called here in order to maintain consistency with phase field literature.

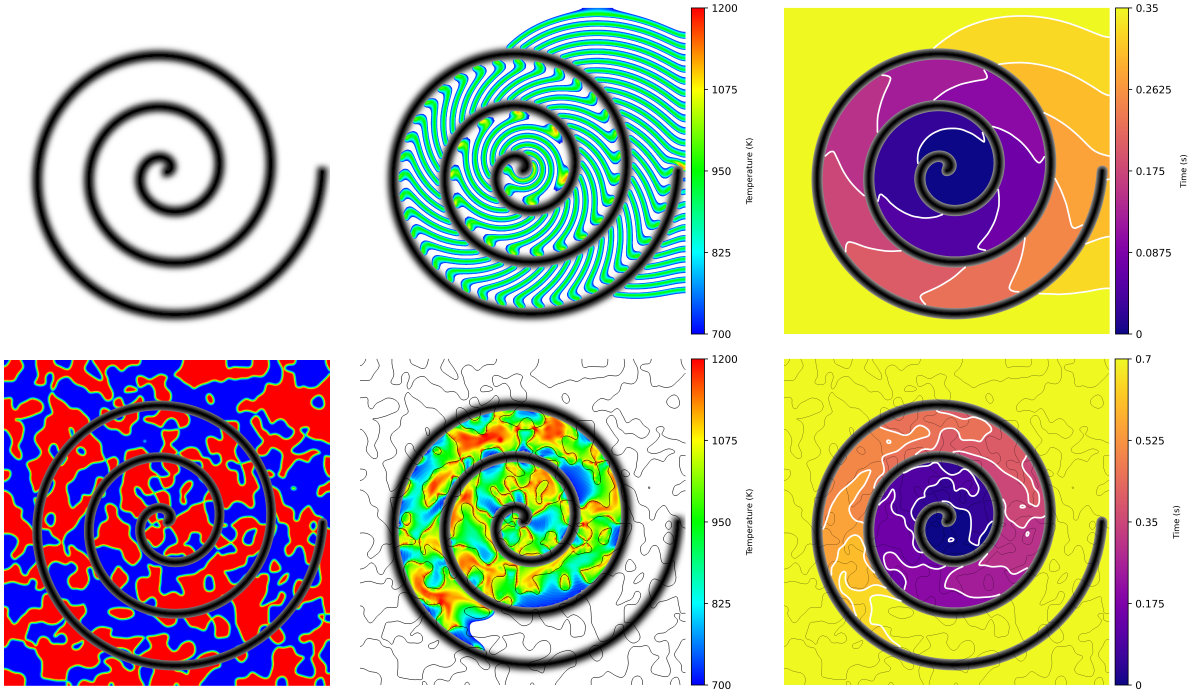

Figure 3: Output temperatures and burn contours of the spiral void and random placement of AP in HTPB binder with the spiral void. (top) Configuration with spiral void and constant $\phi = 0.5$. (bottom) Configuration with spiral and artificial ϕ grain. (left) The initial ϕ field (blue/red) and η field (black). The blue areas are HTPB, and the red areas are AP. The black regions are the initial void. (middle) Compiled temperature plot of the highest temperature value at each point over the entire simulation length. The temperature is highest in the HTPB binder, similar to the previous result without the spiral void. (right) Contours of the η field during regression. The surface movement rate is slower and has more distant geometry because there are distant AP and HTPB regions compared to setting $\phi = 0.5$ everywhere, which assumes a homogeneous mixture with AP and HTPB, increasing burn rate.

according to the same full-feedback kinetics used for the external burn front. If the mesh is sufficiently refined to capture the smallest radius of curvature of interest, this stabilized formulation can be applied to more general voided mesostructures. Consequently, processed experimental images can be used as model inputs to investigate deflagration behavior in performance-grade propellants or propellants that have undergone damage or decomposition.

3.2. Experimental mesostructure

Having established that the stabilized formulation can preserve a highly curved void surface until it is thermally activated, the model is next applied to an experimentally observed mesostructure. This case tests whether an image-derived AP/HTPB morphology with irregular particle boundaries and surface porosity can be used directly to analyze local thermal and mechanical response. A scanning electron microscope image of an AP/HTPB propellant containing porous AP particles [12] is processed into initial ϕ and η fields and used as the model input. These porous particles were produced by introducing bubbles during drying, which resulted in small voids on particle surfaces. Although the presence of such voids is known to increase burn rate, the local thermal and mechanical mechanisms underlying that increase remain difficult to observe experimentally. The selected image is approximately 110 µm by 80 µm; after processing, the domain contains approximately 4% void by area (Fig. 4).

During deflagration, the highest temperature occurs near the laser initiation boundary, while moderate to high temperatures develop throughout regions where AP and HTPB are well mixed. Lower maximum temperatures occur near AP-rich regions and near larger voids. The AP-rich region burns more rapidly, leaving less time for heat accumulation in the condensed phase, while voids remove energetic material and interrupt local heat storage. These spatial temperature variations are important because they generate nonuniform thermal expansion in the solid, producing internal stresses in addition to those caused by the pressure surface traction (Fig. 5).

The mechanical response shows stress concentrations near voids, consistent with prior analyses of voided propellant microstructures [72]. For this image-derived case, the maximum von Mises stress is 434.7 kPa and the maximum strain is 14.3%. Reported ultimate strengths for HTPB propellants span approximately 0.4 MPa to 2.0 MPa, with failure strains between 20% and 50% depending on loading and environmental conditions [73]. The predicted stresses and strains therefore do not establish failure, but they indicate that void-induced thermal and pressure loading can drive the local mechanical state toward experimentally relevant limits. Because direct validation data for subsurface stress fields at

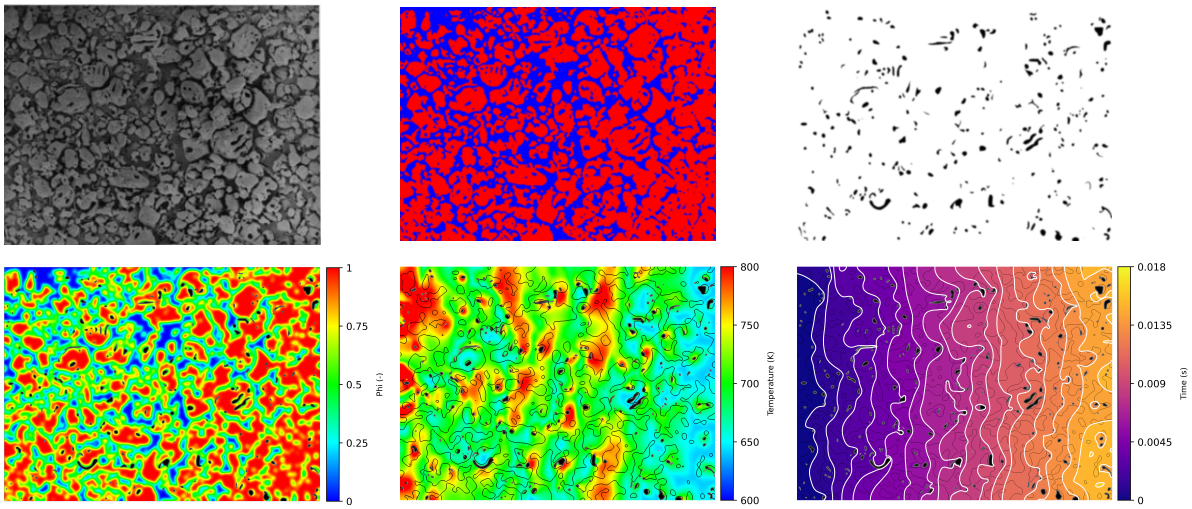

Figure 4: Experimental image processing and simulated burn of processed porous propellant (Sample A). (top) Experimental image processing steps). (left) Initial unprocessed image with voids [15]. (middle) Processed initial ϕ field where red is AP and blue is HTPB. (right) Processed η field where black regions are voids. (bottom) Simulated burn results. (left) Initial AP/HTPB (red/blue) and voids (black). (middle) Compiled highest temperature at each timestep over the simulation. (right) η field surface contours. As the propellant burns the temperature is lowest on the right where there is the most AP because AP burns faster than HTPB, so there is less time for heat to build up in the domain.

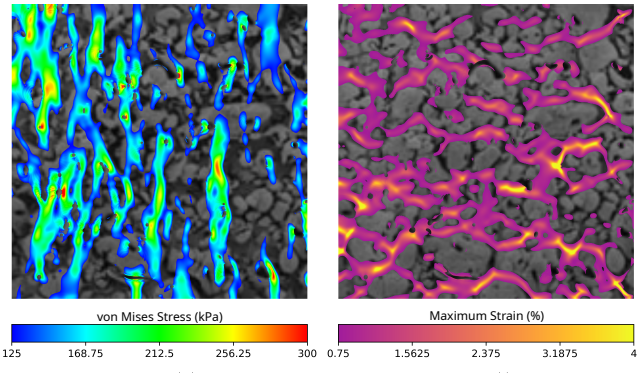

Figure 5: Superimposed maximum von Mises stress and maximum strain in propellant after a simulated burn at 1 MPa. The voids induce stress concentrations in the propellant, and the maximum strain occurs in the HTPB binder. A square (58.5 µm by 58.5 µm) domain is used to improve the stability of the elastic solver.

this length scale are limited, these mechanical results are treated as predictive diagnostics rather than validated failure predictions.

3.3. Validation: porous / hollow AP particles

The preceding cases show that the stabilized formulation can treat complex and image-derived void morphologies. The model is now compared with experimental burn-rate measurements for AP/HTPB propellants containing porous, hollow, and void-free AP particles [15]. Prior work validated the same full-feedback framework without voids using AP/HTPB sandwich flames, spherical packing configurations [46], and realistic mesostructures [38]; the present comparison tests whether the cutoff-stabilized formulation preserves that predictive capability when internal void surfaces are introduced.

Table 2
Sauter mean diameter (SMD) and mean diameter (MD) of AP particles and voids used to match experimental propellant samples.

	AP Particles		Voids		
	SMD (µm)	std	MD (µm)	std	(%)
A	7.73	0.752	0.572	0.264	11.00
B	4.56	0.405	0.343	0.152	6.00
C	5.34	0.474	0.403	0.180	6.00
D	4.36	0.394	0.327	0.147	7.00
E	8.19	0.740	0.617	0.275	7.00
F	8.66	0.787	0.649	0.290	6.00
G	3.42	0.341	0.673	0.148	14.00
H	3.78	0.375	0.725	0.158	13.00
I	3.03	0.274	0.000	0.000	0.00
J	3.79	0.341	0.000	0.000	0.00
K	3.69	0.334	0.000	0.000	0.00
R	14.87	1.277	0.000	0.000	0.00
S	7.80	0.711	0.000	0.000	0.00
T	2.83	0.256	0.000	0.000	0.00

Because the experimental samples are three-dimensional and the present simulations are two-dimensional mesoscale surrogates, the comparison is constructed to match the dominant geometric descriptors rather than each particle exactly. AP particles are represented as spheres in the experimental statistics and disks in the two-dimensional computational domains. Hollow particles contain a single scaled concentric void, while porous particles contain multiple

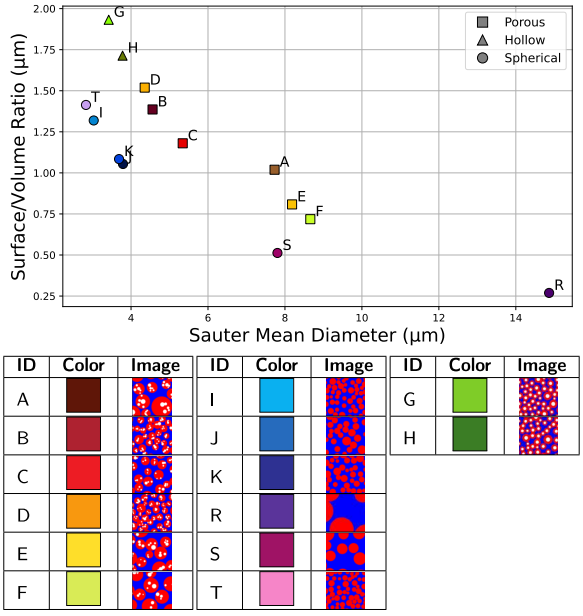

Figure 6: (left) comparison of the surface area to volume ratio of mesostructures as the diameter changes. Decreasing the diameter or increasing the void fraction increases the surface area. (right) Legend with example plots of the different mesostructures.

randomly placed voids with a median radius of approximately 15% of that of the parent particle. All samples are generated to match the experimental AP mass fraction of 72%, which corresponds to approximately $55-60\%$ AP by volume depending on void fraction. The Sauter mean diameter ($\text{SMD} = \sum_{i=1}^{N} d_i^3 / \sum_{i=1}^{N} d_i^2$) of AP particles is used to match the approximate weight mean diameter of the experimental datasets (Fig. 6 and Table 2).

For a fixed AP loading, both particle diameter and void fraction influence regression rate by changing the amount of exposed solid-gas interfacial area. For comparison across samples, these effects are collapsed into a particle surface-area-to-volume ratio. The ratio is found,

$$\frac{\text{SA}}{\text{Vol.}} = \frac{2(\text{AP}_{\text{SMD}} + \text{Void}_{\text{MD}} \cdot \text{Mean Num. Voids})}{\left(\text{AP}_{\text{SMD}}^2 - \text{Void}_{\text{MD}}^2 \cdot \text{Mean Num. Voids}\right)} \tag{16}$$

where AP_{SMD} is the Sauter mean diameter of the AP particles and Void_{MD} is the mean diameter of the voids. The surface-area-to-volume ratio increases with increased void fraction or decreased particle diameter (Fig. 6 and Table 2). The experimental void fraction is defined as the total volume of a 3D sample occupied by voids. For the 2D surrogate packings used in this work, the same particle diameter distributions are used and void volume fraction is approximated by void area fraction.

Regression modeling with packed surrogate mesostructures is performed at 1 MPa and 7 MPa gauge pressure (1.1 MPa and 7.1 MPa absolute pressure). All experimental data presented are from previous research by Kohga [15], and all burn rates used during analysis are provided (Appendix C). The mean burn rate and 95% upper and lower

Table 3
Numerical parameters used during experimental comparison.

Parameter Name	Value
η Diffuse Thickness (μm)	1.0
ϕ Diffuse Thickness (μm)	1.5
X Direction Base Number of Cells (-)	128
X Direction Domain Length (μm)	200
Y Direction Base Number of Cells (-)	16
Y Direction Domain Length (μm)	25
Number of AMR levels (no voids) (μm)	3
Number of AMR levels (voids) (μm)	4
Number of cell divisions per level (-)	2
Timestep (ns)	200
Plot Interval (μs)	800
Burn Area Diffuse Thickness (μm)	1.0
Interface Width (ζ), Spherical/Hollow (μm)	23.0
Interface Width (ζ), Porous Particles (μm)	63.0

instantaneous burn rates are computed after removing the first and last 5 data points due to transient effects from the laser and inlet/outlet boundary conditions. For all results, numerical parameters are held constant except for ζ (Table 3), which is changed between porous and hollow AP particles to account for the different characteristic length scales of their void surfaces. ζ is set to 23 μm for hollow and spherical particles and 63 μm for porous particles.

At 1 MPa, the model captures the experimental burn rates for all considered geometries within 28% error (Table C.1). For mesostructures without voids, the predicted trend follows the experimental data, although the model over-predicts the influence of particle size. When voids are added, the porous-particle cases show a weak decrease in regression rate as surface-area-to-volume ratio increases (Fig. 7). This behavior reflects competing effects: voids increase exposed interfacial area, but they also remove energetic material and locally reduce heat accumulation. In the diffuse representation, a small amount of AP is also removed when the η field is applied around void surfaces. Because AP contributes strongly to the local heat flux, this reduction lowers the maximum attainable condensed-phase temperature. The porous mesostructures reach maximum temperatures between 750 K and 800 K, while spherical mesostructures exceed 1000 K; thus, the acceleration associated with added void surface area can be offset by reduced local temperature and lower available energetic material.

The instantaneous burn-rate bounds also narrow as surface-area-to-volume ratio increases. Mesostructures with smaller AP particles are closer to a homogeneous mixture, producing more consistent local burn rates. In contrast, mesostructures with larger AP particles, particularly samples R and S, remain more heterogeneous and therefore exhibit a wider range of instantaneous burn rates (Fig. 8).

At 7 MPa, the same numerical parameters are retained and only the pressure is increased. The comparison is less quantitative than at 1 MPa, with larger errors in several cases (Table C.2), but the model still captures qualitative trends.

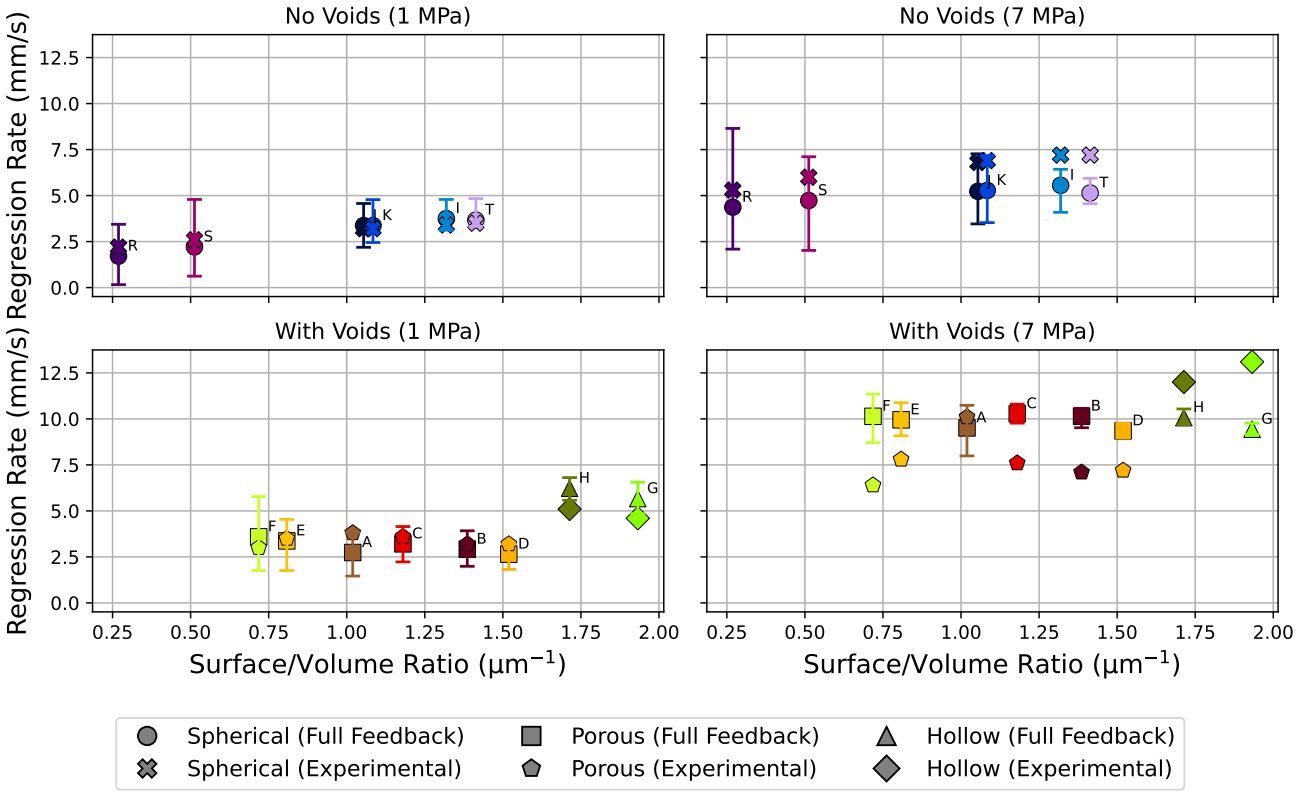

Figure 7: Low pressure regression rates compared to experimental data. (left) Spherical particles with voids. (right) Porous and hollow particles with voids. The upper and lower bounds on the computational regression rate fall within the experimental burn rate for all the spherical and porous particles at low pressures.

For void-free samples, the regression rate increases with surface-area-to-volume ratio, while porous samples retain a weak decrease in regression rate as surface-area-to-volume ratio increases. The narrower instantaneous burn-rate spread at 7 MPa suggests that faster overall regression reduces the relative influence of local heterogeneity, especially for small-particle mesostructures.

The high-pressure discrepancy points to missing heat-transfer physics rather than failure of the cutoff stabilization. As pressure increases from 1 MPa toward 10 MPa, the flame front shifts closer to the propellant surface and maximum gas-phase temperatures increase [53]. Radiative heat transfer scales strongly with temperature and increases as the flame approaches the surface, so neglecting radiation can underpredict the effective surface heating at elevated pressure. Future high-pressure extensions should therefore include radiative or more explicit gas-phase heat-transfer models rather than relying solely on the present pressure-scaled heat-flux surrogate.

4. Conclusion

In this work, previously developed diffuse interface methods are applied to arbitrary mesostructure geometries and extended to demonstrate the effect of voids on SCP regression rates by comparing solid, porous, and hollow AP particles. Unlike surface mapping or level-set methods, which can struggle to capture complex evolving geometries, the phase-field approach naturally handles arbitrary geometries for both propellant grains and voids. This capability is demonstrated through the use of a randomized grain structure with a central spiral void, as well as an experimental SEM photograph.

The model is validated against experimental data and shown to capture relevant trends reliant on particle size and specific surface area with reasonable accuracy. The model agrees with experimental data within 28% error at 1 MPa, and reflects general trends at 7 MPa. The model over-predicts the effect of increased surface area with the introduction of voids at the higher pressure, but captures the general behavior demonstrated experimentally. Future research areas include modeling the fluid phase during regression to capture the effects of hot gases on voids, and radiation heat transfer which becomes more prevalent at higher temperatures.

These results suggest that the diffuse interface method can be applied to reliably assist in screening candidate SCP geometries and compositions prior to experimental studies, helping to reduce iteration costs and accelerate the development of future SCPs.

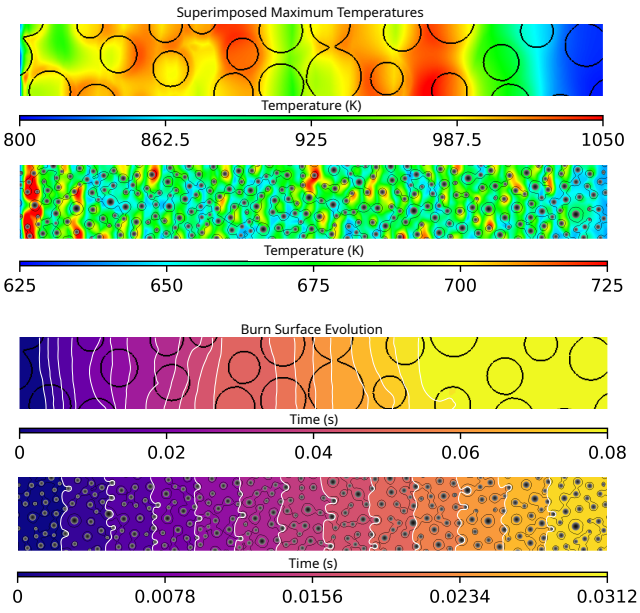

Figure 8: (top) Composite temperature of spherical sample R and hollow sample H, black contour lines are drawn at $\phi = 0.7$. (bottom) Regression contours of Samples R and H, white lines differentiate regression contours. The maximum temperature in sample R is much higher than sample H, but sample R regresses slower because of a lower surface area to volume ratio.

Novelty and significance statement

It is significant to investigate the effects of voids inside SCPs for the development, use, and safety of propellants. Previous work had shown the substantial impact voids have on the regression rate of SCPs, but had not explored the reasons for this regression rate increase. A model is benchmarked against experimental data and used to provide thermal mechanical analysis of AP/HTPB deflagration with voids of any arbitrary shape or location inside the microstructure.

CrediT authorship contribution statement

Caleb Munger: Data curation, Investigation, Methodology, Software, Validation, Visualization, Writing – original draft, Writing – review and editing. **Jenna Stocker**: Data curation, Investigation, Software, Validation, Visualization, Writing – original draft, Writing – review and editing. **Eric Sandall**: Conceptualization, Supervision, Writing – review and editing. **Brandon Runnels**: Conceptualization, Funding acquisition, Project administration, Resources, Supervision, Writing – review and editing.

Declaration of competing interest

The authors declare that they have no known competing financial interests or personal relationships that could have appeared to influence the work reported in this paper.

Acknowledgments

Authors CM and BR acknowledge support from the Office of Naval Research, United States, grant number N00014-25-1-2029. Authors JS and BR also gratefully acknowledge support from the Air Force Research Laboratory. Author ES acknowledges support from the SMART Scholarship and NAWCWD Fellowship. The authors acknowledge Dr. Kamran B. Ghiassi at AFRL Edwards for insightful discussions regarding this work.

References

[1] Luigi T. DeLuca, "Highlights of Solid Rocket Propulsion History", *Chemical Rocket Propulsion: A Comprehensive Survey of Energetic Materials*, ed. by Luigi T. De Luca, Toru Shimada, Valery P. Sinditskii, and Max Calabro, Cham: Springer International Publishing, 2017, pp. 1015–1032, ISBN: 978-3-319-27748-6, DOI: 10.1007/978-3-319-27748-6_42, URL: https://doi.org/10.1007/978-3-319-27748-6_42 (visited on 01/13/2026).

[2] Shalini Chaturvedi and Pragnesh N. Dave, Solid Propellants: AP/HTPB Composite Propellants, Arabian Journal of Chemistry 12.8 (Dec. 1, 2019), 2061–2068, ISSN: 1878-5352, DOI: 10.1016/j.arabjc.2014.12.033, URL: https://www.sciencedirect.com/science/article/pii/S1878535215000106 (visited on 01/13/2026).

[3] Weiqiang Pang, Xu Xia, Yu Zhao, Luigi T. DeLuca, Djalal Trache, Dihua OuYang, Saiqin Meng, Xiaogang Liu, and Hongjian Yu, Effect of Carbon Nanotubes (CNTs) on the Performance of Solid Rocket Propellants (SRPs): A Short Review, FirePhysChem, Energetic Materials for Propulsion Applications 3.3 (Sept. 1, 2023), 227–233, ISSN: 2667-1344, DOI: 10.1016/j.fpc.2023.05.003, URL: https://www.sciencedirect.com/science/article/pii/S2667134423000287 (visited on 01/13/2026).

[4] Wen Ao, Zhimin Fan, Lu Liu, Yuxin An, Jiaren Ren, Mingtao Zhao, Peijin Liu, and Larry K. B. Li, Agglomeration and Combustion Characteristics of Solid Composite Propellants Containing Aluminum-Based Alloys, Combustion and Flame 220 (Oct. 1, 2020), 288–297, ISSN: 0010-2180, DOI: 10.1016/j.combustflame.2020.07.004, URL: https://www.sciencedirect.com/science/article/pii/S0010218020302662 (visited on 01/13/2026).

[5] K. Jayaraman, K. V. Anand, D. S. Bhatt, S. R. Chakravarthy, and R. Sarathi, Production, Characterization, and Combustion of Nanoaluminum in Composite Solid Propellants, Journal of Propulsion and Power 25.2 (Mar. 2009), 471–481, ISSN: 0748-4658, 1533-3876, DOI: 10.2514/1.36490, URL: https://arc.aiaa.org/doi/10.2514/1.36490 (visited on 01/13/2026).

[6] George P. Sutton and Oscar Biblarz, *Rocket propulsion elements*, eng, Ninth edition., Hoboken, New Jersey: John Wiley & Sons Inc., 2017, ISBN: 1118753658.

[7] Kelly J. Mathesius, "Manufacturing Methods for a Solid Rocket Motor Propelling a Small, Fast Flight Vehicle", Thesis, Massachusetts Institute of Technology, 2019, URL: https://dspace.mit.edu/handle/1721.1/122377 (visited on 04/01/2026).

[8] Shixiong Song, Jiawei Shi, Quanbin Ren, Kai Miao, Min Tang, and Hongbin Shi, Comparative Study on Extrusion 3D Printing of Solid Propellant Based on Plunger and Screw, Materials 18.4 (Jan. 2025), 777, ISSN: 1996-1944, DOI: 10.3390/ma18040777, URL: https://www.mdpi.com/1996-1944/18/4/777 (visited on 05/18/2026).

[9] M. S. McClain, I. E. Gunduz, and S. F. Son, Additive Manufacturing of Ammonium Perchlorate Composite Propellant with High Solids Loadings, Proceedings of the Combustion Institute 37.3 (Jan. 1, 2019), 3135–3142, ISSN: 1540-7489, DOI: 10.1016/j.proci.2018.05.052, URL: https://www.sciencedirect.com/science/article/pii/S1540748918300531 (visited on 12/15/2025).

[10] Zi-Jie Zou, Hong-Fu Qiang, Yi-Yi Li, and Xue-Ren Wang, Review on the Dewetting of the Particle-Matrix Interface in Composite Solid Propellants, Propellants, Explosives, Pyrotechnics 48.3 (2023),

e202200270, ISSN: 1521-4087, DOI: 10.1002/prep.202200270, URL: https://onlinelibrary.wiley.com/doi/abs/10.1002/prep.202200270 (visited on 12/16/2025).

[11] Gerhard Drolshagen, Impact Effects from Small Size Meteoroids and Space Debris, Advances in Space Research 41.7 (Jan. 1, 2008), 1123–1131, ISSN: 0273-1177, DOI: 10.1016/j.asr.2007.09.007, URL: https://www.sciencedirect.com/science/article/pii/S0273117707009416 (visited on 11/06/2025).

[12] Makoto Kohga, Effect of Voids inside AP Particles on Burning Rate of AP/HTPB Composite Propellant, Propellants, Explosives, Pyrotechnics 33.4 (2008), 249–254, ISSN: 1521-4087, DOI: 10.1002/prep.200700234, URL: https://onlinelibrary.wiley.com/doi/abs/10.1002/prep.200700234 (visited on 12/15/2025).

[13] Manvith Amara, "Performance Variability in Solid Rocket Motors", University of Alamana in Huntsville, May 1, 2022, URL: https://louis.uah.edu/honors-capstones/683.

[14] Harold H. Bradley, Boggs Jr., and Thomas L., *Convective Burning in Propellant Defects: A Literature Review:* Fort Belvoir, VA: Defense Technical Information Center, Feb. 1, 1978, DOI: 10.21236/ADA051867, URL: http://www.dtic.mil/docs/citations/ADA051867 (visited on 04/04/2026).

[15] Makoto Kohga, Burning Characteristics of AP/HTPB Composite Propellants Prepared with Fine Porous or Fine Hollow Ammonium Perchlorate, Propellants, Explosives, Pyrotechnics 31.1 (2006), 50–55, ISSN: 1521-4087, DOI: 10.1002/prep.200600007, URL: https://onlinelibrary.wiley.com/doi/abs/10.1002/prep.200600007 (visited on 02/26/2026).

[16] Ming Lei, Jianjun Wang, Jiming Cheng, Jinyou Xiao, Lihua Wen, Haibao Lu, and Xiao Hou, A Constitutive Model of the Solid Propellants Considering the Interface Strength and Dewetting, Composites Science and Technology 185 (Jan. 5, 2020), 107893, ISSN: 0266-3538, DOI: 10.1016/j.compscitech.2019.107893, URL: https://www.sciencedirect.com/science/article/pii/S026635381932706X (visited on 12/16/2025).

[17] M S Miller, B M Rice, A J Kotlar, and R J Cramer, A New Approach to Propellant Formulation: Minimizing Life-Cycle Costs through Science-Based Design, Clean Products and Processes 2.1 (2000), 37–46.

[18] A. Hegab, T. L. Jackson, J. Buckmaster, and D. S. Stewart, Nonsteady Burning of Periodic Sandwich Propellants with Complete Coupling between the Solid and Gas Phases, Combustion and Flame 125.1 (Apr. 1, 2001), 1055–1070, ISSN: 0010-2180, DOI: 10.1016/S0010-2180(01)00226-7, URL: https://www.sciencedirect.com/science/article/pii/S0010218001002267 (visited on 12/16/2025).

[19] L Massa, T L Jackson, and M Short, Numerical Solution of Three-Dimensional Heterogeneous Solid Propellants, Combustion Theory and Modelling 7.3 (Sept. 2003), 579, ISSN: 1364-7830, DOI: 10.1088/1364-7830/7/3/308, URL: https://doi.org/10.1088/1364-7830/7/3/308 (visited on 10/28/2025).

[20] X Wang, T L Jackson, and L Massa, Numerical Simulation of Heterogeneous Propellant Combustion by a Level Set Method, Combustion Theory and Modelling 8.2 (Mar. 2004), 227, ISSN: 1364-7830, DOI: 10.1088/1364-7830/8/2/003, URL: https://doi.org/10.1088/1364-7830/8/2/003 (visited on 10/28/2025).

[21] Pierre Bernigaud, Dmitry Davidenko, and Laurent Catoire, AP/HTPB heterogeneous combustion with revised kinetics, Proceedings of the Combustion Institute 40.1 (2024), 105469, ISSN: 1540-7489, DOI: https://doi.org/10.1016/j.proci.2024.105469, URL: https://www.sciencedirect.com/science/article/pii/S1540748924002773.

[22] Xing Liu, Quanbin Ren, Qihu Wang, Yuanqi Bai, and Zeyu Li, Investigation on Combustion and Heat Transfer in AP/HTPB Propellants with Multiscale Model Coupling Validated Chemical Kinetics and Representative Microstructure, Applied Thermal Engineering (May 1, 2026), 131274, ISSN: 1359-4311, DOI: 10.1016/j.applthermaleng.2026.131274, URL: https://www.sciencedirect.com/science/article/pii/S1359431126015826 (visited on 05/04/2026).

[23] Matthew L. Gross, Trevor D. Hedman, Steven F. Son, Thomas L. Jackson, and Merrill W. Beckstead, Coupling Micro and Meso-Scale Combustion Models of AP/HTPB Propellants, Combustion and Flame 160.5 (May 1, 2013), 982–992, ISSN: 0010-2180, DOI: 10.1016/j.combustflame.2013.01.016, URL: https://www.sciencedirect.com/science/article/pii/S001021801300031X (visited on 05/04/2026).

[24] K.R. Srinivasan, K. Matouš, P.H. Geubelle, and T.L. Jackson, Thermomechanical Modeling of Regressing Heterogeneous Solid Propellants, Journal of Computational Physics 228.21 (Nov. 2009), 7883–7901, ISSN: 00219991, DOI: 10.1016/j.jcp.2009.07.003, URL: https://linkinghub.elsevier.com/retrieve/pii/S0021999109003775 (visited on 11/05/2025).

[25] Tadbhagya Kumar, Chris H. Rycroft, and Thomas L. Jackson, Eulerian Thermo-Mechanical Simulations of Heterogeneous Solid Propellants Using an Approximate Projection Method, Combustion and Flame 219 (Sept. 1, 2020), 198–211, ISSN: 0010-2180, DOI: 10.1016/j.combustflame.2020.05.023, URL: https://www.sciencedirect.com/science/article/pii/S0010218020302091 (visited on 12/16/2025).

[26] Tadbhagya Kumar and Thomas L. Jackson, Three-Dimensional Thermo-Mechanical Simulations of Heterogeneous Solid Propellants, Combustion and Flame 233 (Nov. 2021), 111590, ISSN: 00102180, DOI: 10.1016/j.combustflame.2021.111590, URL: https://linkinghub.elsevier.com/retrieve/pii/S0010218021003333 (visited on 02/16/2026).

[27] Robin Devillers, Guy Le Besnerais, Matthieu Nugue, and Nathalie Cesco, Experimental Analysis of Solid-Propellant Surface during Combustion with Shadowgraphy Images: New Tools to Assist Aluminum-Agglomeration Modelling (2017), 14 pages, DOI: 10.13009/EUCASS2017-327, URL: https://www.eucass.eu/doi/EUCASS2017-327.pdf (visited on 04/27/2026).

[28] Yu Liao, Bingning Jin, Siying Yang, Jiacheng Li, Peijin Liu, and Yu Guan, Experimental Investigation of Solid Propellants Combustion Response to Pressure Oscillations Using Advanced High-Resolution Diagnostics, Applied Energy 377 (Jan. 2025), 124227, ISSN: 03062619, DOI: 10.1016/j.apenergy.2024.124227, URL: https://linkinghub.elsevier.com/retrieve/pii/S0306261924016106 (visited on 04/27/2026).

[29] T. Decker, R. Devillers, S. Gallier, and J. Anthoine, Agglomeration in Solid Propellants Loaded with Inert Particles Study of Physical Phenomena Using Shadowgraphy Image Processing, Proceedings of the 9th European Conference for Aerospace Sciences (June 27, 2022), 13 pages, DOI: 10.13009/EUCASS2022-4371, URL: https://www.eucass.eu/doi/EUCASS2022-4371.pdf (visited on 04/27/2026).

[30] Hu Ni, Rong Fan, Haihang Hu, Bin Yang, Zhixin Wang, Di Cao, Yang Yang, and Zhiquan Shi, Synchronized Measurement Method of Burning Rate and Combustion Temperature of a Solid Propellant Specimen, Applied Optics 63.13 (May 1, 2024), 3420, ISSN: 1559-128X, 2155-3165, DOI: 10.1364/AO.520172, URL: https://opg.optica.org/abstract.cfm?URI=ao-63-13-3420 (visited on 04/27/2026).

[31] Thomas Decker, Robin Devillers, and Stany Gallier, Agglomeration in Solid Propellants Loaded with Inert Particles Study of Propellant Formulation Influence Using Shadowgraphy Image Processing (2023), 15 pages, DOI: 10.13009/EUCASS2023-415, URL: https://www.eucass.eu/doi/EUCASS2023-415.pdf (visited on 04/27/2026).

[32] Yu Cang and Lipo Wang, Understanding AP/HTPB composite propellant combustion from new perspectives, Combustion and Flame 259 (2024), 113108, ISSN: 0010-2180, DOI: https://doi.org/10.1016/j.combustflame.2023.113108, URL: https://www.sciencedirect.com/science/article/pii/S0010218023004832.

[33] Kaixuan Chen, Xiaochun Xue, and Yonggang Yu, Modeling Transient Combustion and Regression Behavior of NEPE Propellant Based on Random Particle Packing, Applied Mathematical Modelling 126 (Feb. 1, 2024), 85–104, ISSN: 0307-904X, DOI: 10.1016/j.apm.2023.10.036, URL: https://www.sciencedirect.com/science/article/pii/S0307904X23004961 (visited on 04/04/2026).

[34] Frederic Gibou, Ronald Fedkiw, and Stanley Osher, A review of level-set methods and some recent applications, Journal of Computational Physics 353 (2018), 82–109, ISSN: 0021-9991, DOI: https://doi.org/10.1016/j.jcp.2017.10.006, URL: https://www.sciencedirect.com/science/article/pii/S0021999117307441.

[35] Daniel Hartmann, Matthias Meinke, and Wolfgang Schröder, Differential Equation Based Constrained Reinitialization for Level Set Methods, Journal of Computational Physics 227.14 (July 1, 2008), 6821–6845, ISSN: 0021-9991, DOI: 10.1016/j.jcp.2008.03.040, URL: https://www.sciencedirect.com/science/article/pii/S0021999108001964 (visited on 04/29/2026).

[36] Vimal Ramanuj and Ramanan Sankaran, High Order Anchoring and Reinitialization of Level Set Function for Simulating Interface Motion, Journal of Scientific Computing 81.3 (Dec. 1, 2019), 1963–1986, ISSN: 1573-7691, DOI: 10.1007/s10915-019-01076-0, URL: https://doi.org/10.1007/s10915-019-01076-0 (visited on 04/29/2026).

[37] Baburaj Kanagarajan, John M. Quinlan, and Brandon Runnels, A Diffuse Interface Method for Solid-Phase Modeling of Regression Behavior in Solid Composite Propellants, Combustion and Flame 242 (Aug. 1, 2022), 112219, ISSN: 0010-2180, DOI: 10.1016/j.combustflame.2022.112219, URL: https://www.sciencedirect.com/science/article/pii/S0010218022002346 (visited on 04/04/2026).

[38] Maycon Meier, Emma Schmidt, Patrick Martinez, J. Matt Quinlan, and Brandon Runnels, Diffuse Interface Method for Solid Composite Propellant Ignition and Regression, Combustion and Flame 259 (Jan. 1, 2024), 113120, ISSN: 0010-2180, DOI: 10.1016/j.combustflame.2023.113120, URL: https://www.sciencedirect.com/science/article/pii/S0010218023004959 (visited on 11/04/2025).

[39] F. Ponti, S. Mini, and A. Annovazzi, Numerical Evaluation of the Effects of Inclusions on Solid Rocket Motor Performance, AIAA Journal 58.9 (2020), 4028–4036, ISSN: 0001-1452, DOI: 10.2514/1.J058735, URL: https://doi.org/10.2514/1.J058735 (visited on 04/04/2026).

[40] F Ponti, S Mini, L Fadigati, V Ravaglioli, A Annovazzi, and V Garreffa, Effects of Inclusions on the Performance of a Solid Rocket Motor, Acta Astronautica 189 (2021), 283–297.

[41] Juan Tizon and Efren Benavides, General Burnback Analysis for Anisotropic and Heterogeneous Solid Propellants, Journal of Propulsion and Power 40.5 (2024), 769–780, DOI: 10.2514/1.B39444, URL: https://arc.aiaa.org/doi/epdf/10.2514/1.B39444 (visited on 04/04/2026).

[42] Brian C Barnes, Daniel C Elton, Zois Boukouvalas, DeCarlos E Taylor, William D Mattson, D Fuge, and Peter W Chung, "Machine Learning of Energetic Material Properties", 2018, arXiv: 1807.06156.

[43] Brian C. Barnes, "Deep Learning for Energetic Material Detonation Performance", TRANSPORT, ECOLOGY - SUSTAINABLE DEVELOPMENT EKO VARNA 2024, Varna, Bulgaria, 2020, p. 070002, DOI: 10.1063/12.0001089, URL: https://pubs.aip.org/aip/acp/article-lookup/doi/10.1063/12.0001089 (visited on 04/23/2026).

[44] Geng Xu, Zilong Zhao, Jiangyuan Li, Jieyao Lyu, Bingning Jin, Peijin Liu, and Wen Ao, NeuroFire: Application of Neural Networks for Multi-Scale Combustion Performance Simulation in Solid Composite Propellants, Fuel 402 (Dec. 15, 2025), 136008, ISSN: 0016-2361, DOI: 10.1016/j.fuel.2025.136008, URL: https://www.sciencedirect.com/science/article/pii/S0016236125017338 (visited on 04/04/2026).

[45] Wei-Che Lin, Luca Massa, and Gregory Young, Modeling of the Heterogeneous Hypergolic Ignition with Particle Packing Model, Combustion and Flame 260 (Feb. 1, 2024), 113251, ISSN: 0010-2180, DOI: 10.1016/j.combustflame.2023.113251, URL: https://www.sciencedirect.com/science/article/pii/S0010218023006259 (visited on 04/22/2026).

[46] Maycon Meier and Brandon Runnels, Finite Kinematics Diffuse Interface Mechanics Coupled to Solid Composite Propellant Deflagration, Computer Methods in Applied Mechanics and Engineering 427 (July 1, 2024), ISSN: 0045-7825, DOI: 10.1016/j.cma.2024.117040, URL: https://www.sciencedirect.com/science/article/pii/S0045782524002962 (visited on 10/27/2025).

[47] J.K. Chen and T.B. Brill, Chemistry and Kinetics of Hydroxyl-Terminated Polybutadiene (HTPB) and Diisocyanate-HTPB Polymers during Slow Decomposition and Combustion-like Conditions, Combustion and Flame 87.3–4 (Dec. 1991), 217–232, ISSN: 00102180, DOI: 10.1016/0010-2180(91)90109-0, URL: https://linkinghub.elsevier.com/retrieve/pii/001021809190109O (visited on 03/23/2026).

[48] Claresta Dennis and Brian Bojko, On the Combustion of Heterogeneous AP/HTPB Composite Propellants: A Review, Fuel 254 (Oct. 15, 2019), 115646, ISSN: 0016-2361, DOI: 10.1016/j.fuel.2019.115646, URL: https://www.sciencedirect.com/science/article/pii/S0016236119309986 (visited on 02/18/2026).

[49] Muhammad Irfan and Ji Jun Xiao, Thermal Degradation Behavior of Thermally-Oxidized Hydroxyl-Terminated Polybutadiene (HTPB): An Assessment of Thermal Stability, ChemistrySelect 9.40 (2024), e202402278, ISSN: 2365-6549, DOI: 10.1002/slct.202402278, URL: https://onlinelibrary.wiley.com/doi/abs/10.1002/slct.202402278 (visited on 04/22/2026).

[50] Mahi Gokuli and Brandon Runnels, Multiphase Field Modeling of Grain Boundary Migration Mediated by Emergent Disconnections, Acta Materialia 217 (Sept. 15, 2021), 117149, ISSN: 1359-6454, DOI: 10.1016/j.actamat.2021.117149, URL: https://www.sciencedirect.com/science/article/pii/S1359645421005292 (visited on 04/28/2026).

[51] Yang Hu, Dennis M. Kochmann, and Brandon Runnels, Atomistic Informed Phase Field Modeling of Magnesium Twin Growth by Disconnections, Acta Materialia 284 (Jan. 1, 2025), 120564, ISSN: 1359-6454, DOI: 10.1016/j.actamat.2024.120564, URL: https://www.sciencedirect.com/science/article/pii/S1359645424009121 (visited on 04/28/2026).

[52] Laurent Guin and Dennis M. Kochmann, A Phase Field Model for Ferroelectrics with General Kinetics, Part I: Model Formulation, Journal of the Mechanics and Physics of Solids 176 (July 1, 2023), 105301, ISSN: 0022-5096, DOI: 10.1016/j.jmps.2023.105301, URL: https://www.sciencedirect.com/science/article/pii/S0022509623001059 (visited on 04/28/2026).

[53] Matthew Gross and Merrill Beckstead, Steady State Combustion Mechanisms of Ammonium Perchlorate Composite Propellants, Journal of Propulsion and Power 27.5 (2011), 1064–1078, URL: https://arc.aiaa.org/doi/10.2514/1.B34053 (visited on 04/02/2026).

[54] K. Matouš, H. M. Inglis, X. Gu, D. Rypl, T. L. Jackson, and P. H. Geubelle, Multiscale Modeling of Solid Propellants: From Particle Packing to Failure, Composites Science and Technology 67.7 (June 1, 2007), 1694–1708, ISSN: 0266-3538, DOI: 10.1016/j.compscitech.2006.06.017, URL: https://www.sciencedirect.com/science/article/pii/S026635380600234X (visited on 10/28/2025).

[55] L. De Luca, Edward W. Price, and Martin Summerfield, *Nonsteady Burning and Combustion Stability of Solid Propellants*, District of Columbia, United States: Washington, D.C. : American Institute of Aeronautics and Astronautics, 1992, ISBN: 1-56347-014-4, URL: https://searchworks.stanford.edu/view/in00000256178.

[56] Robert Kellogg, Saul Lapidus, Trevor Hedman, and Joseph Kalman, Synchrotron Based Measurement of the Temperature Dependent Thermal Expansion Coefficient of Ammonium Perchlorate, Propellants, Explosives, Pyrotechnics 45.3 (2020), 480–485, ISSN: 1521-4087, DOI: 10.1002/prep.201900257, URL: https://onlinelibrary.wiley.com/doi/abs/10.1002/prep.201900257 (visited on 10/23/2025).

[57] Katarzyna Ganczyk-Specjalska and Paulina Magnuszewska, An Analysis of the Mechanical Properties of HTPB-propellants Using DMA, Materialy Wysokoenergetyczne 12.2 (2020), 81–91.

[58] Makota Kohga, Robert A. Frederick, and Marlow D. Moser, Ultrasonic Properties of Propellant Ingredients, Journal of Propulsion and Power 20 (2004), 135–140, URL: https://api.semanticscholar.org/CorpusID:120085356.

[59] B.O. Reese, J.H. Blackburn, L.B. Slely, and M.W. Evans, Longitudinal sound velocities of granular compacts of ammonium perchlorate and potassium chloride, Combustion and Flame 11.3 (1967), 262–264, ISSN: 0010-2180, DOI: https://doi.org/10.1016/0010-2180(67)90056-9, URL: https://www.sciencedirect.com/science/article/pii/0010218067900569.

[60] Tony Marshall, John Evans, and Robert Frederick, "UAH Solid Propellant Characterization", *43rd AIAA/ASME/SAE/ASEE Joint Propulsion Conference & Exhibit*, DOI: 10.2514/6.2007-5763, eprint: https://arc.aiaa.org/doi/pdf/10.2514/6.2007-5763, URL: https://arc.aiaa.org/doi/abs/10.2514/6.2007-5763.

[61] R. S. Rivlin, Large Elastic Deformations of Isotropic Materials IV. Further Developments of the General Theory, Philosophical Transactions of the Royal Society of London, Series A: Mathematical and Physical Sciences 241.835 (Oct. 5, 1948), 379–397, ISSN: 0080-4614, DOI: 10.1098/rsta.1948.0024, URL: https://doi.org/10.1098/rsta.1948.0024 (visited on 04/30/2026).

[62] R. S. Rivlin and D. W. Saunders, Large Elastic Deformations of Isotropic Materials VII. Experiments on the Deformation of Rubber, Philosophical Transactions of the Royal Society of London. Series A, Mathematical and Physical Sciences 243.865 (Apr. 24, 1951), 251–288, ISSN: 0080-4614, 2054-0272, DOI: 10.1098/rsta.1951.0004, URL: https://royalsocietypublishing.org/rsta/article/243/865/251/44151/Large-elastic-deformations-of-isotropic-materials (visited on 04/30/2026).

[63] Brandon Runnels, Vinamra Agrawal, and Maycon Meier, The Alamo Multiphysics Solver for Phase Field Simulations with Strong-Form Mechanics and Block Structured Adaptive Mesh Refinement, Journal of Open Source Software 10.116 (Dec. 2, 2025), 8581, ISSN: 2475-9066, DOI: 10.21105/joss.08581, URL: https://joss.theoj.org/papers/10.21105/joss.08581 (visited on 01/14/2026).

[64] Weiqun Zhang, Ann Almgren, Vince Beckner, John Bell, Johannes Blaschke, Cy Chan, Marcus Day, Brian Friesen, Kevin Gott, Daniel Graves, Max P. Katz, Andrew Myers, Tan Nguyen, Andrew Nonaka, Michele Rosso, Samuel Williams, and Michael Zingale, AMReX: A Framework for Block-Structured Adaptive Mesh Refinement, Journal of Open Source Software 4.37 (May 12, 2019), 1370, ISSN: 2475-9066, DOI: 10.21105/joss.01370, URL: https://joss.theoj.org/papers/10.21105/joss.01370 (visited on 11/03/2025).

[65] Emma Schmidt, Matt Quinlan, and Brandon Runnels, Self Similar Diffuse Boundary Method for Phase Boundary Driven Flow, Physcis of Fluids 34.11 (2022), DOI: 10.1063/5.010773.

[66] R. Courant, K. Friedrichs, and H. Lewy, On the Partial Difference Equations of Mathematical Physics, IBM Journal of Research and Development 11.2 (Mar. 1967), 215–234, ISSN: 0018-8646, DOI: 10.1147/rd.112.0215, URL: https://ieeexplore.ieee.org/abstract/document/5391985 (visited on 04/06/2026).

[67] Kohei Ozawa, Han-wei Wang, Takefumi Inenaga, and Nobuyuki Tsuboi, "Accuracy of Real-time Fuel Regression Measurement Function of a 3D Printed Solid Fuel", *AIAA Propulsion and Energy 2020 Forum*, American Institute of Aeronautics and Astronautics, 2020, DOI: 10.2514/6.2020-3741, URL: https://arc.aiaa.org/doi/abs/10.2514/6.2020-3741 (visited on 01/16/2026).

[68] given-i=RE family=Fitch given=RE, given-i=JL family=Guenther given=JL, and given-i=JD family=Kilgroe given=JD, *An Evaluation of Aft-End Ignition for Solid Propellant Rocket Motors*, Contractor Report 72447, Cleveland, Ohio: NASA, 1968.

[69] Hank Childs, Eric Brugger, Brad Whitlock, Jeremy Meredith, Sean Ahern, David Pugmire, Kathleen Biagas, Mark Miller, Harrison Cyrus, Weber Gunther, Hari Krishnan, Thomas Fogal, Allen Sanderson, Christoph Garth, E. Wes Bethel, David Camp, Oliver Rubel, Marc Durant, Jean Favre, and Paul Navratil, "VisIt: An End-User Tool For Visualizing and Analyzing Very Large Data", *High Performance Visualization–Enabling Extreme-Scale Scientific Insight*, Oct. 2012, pp. 357–372, DOI: 10.1201/b12985.

[70] Lars Blatny, Henning Löwe, and Johan Gaume, GRFsaw: A Lightweight Stochastic Microstructure Generator, arXiv.org (Dec. 6, 2024), URL: https://arxiv.org/abs/2412.05168v1 (visited on 04/05/2026).

[71] Kyle E. Uhlenhake, Mateo Gomez, Diane N. Collard, Metin Örnek, and Steven F. Son, Laser Ignition of Solid Propellants Using Energetic nAl-PVDF Optical Sensitizers, Combustion and Flame 254 (Aug. 1, 2023), 112848, ISSN: 0010-2180, DOI: 10.1016/j.combustflame.2023.112848, URL: https://www.sciencedirect.com/science/article/pii/S0010218023002298 (visited on 12/19/2025).

[72] T. Davis, D. Healy, A. Bubeck, and R. Walker, Stress Concentrations around Voids in Three Dimensions: The Roots of Failure, Journal of Structural Geology 102 (Sept. 1, 2017), 193–207, ISSN: 0191-8141, DOI: 10.1016/j.jsg.2017.07.013, URL: https://www.sciencedirect.com/science/article/pii/S0191814117301542 (visited on 04/07/2026).

[73] Chengfeng Wu, Yingying Lu, Ming Jiang, Shaoqing Hu, Hongtao Yang, Xiaolong Fu, and Hongyan Li, Study on Mechanical Properties and Failure Mechanisms of Highly Filled Hydroxy-Terminated Polybutadiene Propellant under Different Tensile Loading Conditions, Polymers 15.19 (Jan. 2023), 3869, ISSN: 2073-4360, DOI: 10.3390/polym15193869, URL: https://www.mdpi.com/2073-4360/15/19/3869 (visited on 04/30/2026).

A. Mesh and Time Step Convergence

While this model has shown good agreement with experimental data in the past, it has never been used to simulate regression in SCPs with voids, so care was taken to investigate the mesh and time step sensitivity in a domain with voids. Before comparing to experimental data, mesh and time step convergence studies are used to ensure the regression rate is being precisely measured. A domain of packed AP spheres inside an HTPB binder with spherical voids is used for numerical verification (Fig. A.1). This domain is representative of experimental domains similar to those from Section 3, allowing for a good comparison, while have fewer cells compared to the experimental mesostructures, easing computational cost.

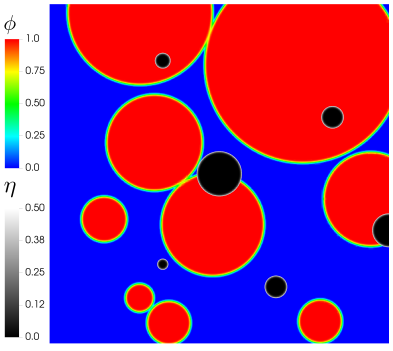

Figure A.1: Initial fields for the mesh convergence study with particles of AP inside an HTPB binder (ϕ field), along with placed voids (η field). The domain is 0.3 x 0.3 mm.

Due to the nature of adaptive mesh refinement, additional refinement levels are utilized to efficiently use computational resources. For these studies, a domain of 300 µm by 300 µm is used, with a base mesh of 8 cells in the x and y direction. Refinement levels 2, 3, 4, and 5 are used to determine the required mesh size. Each refinement level doubles the number of cells inside the refined area in each coordinate direction (i.e. 4x the number of cells in 2D and

8x in 3D). Simulations with refinement levels below 3 were unsuccessful so only data from levels 3, 4, and 5 are analyzed (Table A.1).

Table A.1
Regression rate of the solid propellant at different mesh resolutions.

Max AMR Level	Avg. Regression Rate (mm/s)	Relative Change (%)
3	21.208	
4	9.857	-53.510
5	10.549	6.560
6	10.540	-0.085

The regression rate has negligible dependence on the time step. Time steps of 2000 ns, 1000 ns, 500 ns, and 250 ns seconds are tested. Time steps larger than 2000 ns for the given domain did not progress to completion. Below a timestep of 2000 ns, halving the timestep causes a relative change in the regression rate of the order $1 \cdot 10^{-6}$. As such, it can be concluded that relative to the mesh size, the timestep does not influence the convergence of the regression rate as long as the Courant-Friedrichs-Lewy (CFL) condition is met. For experimental validation, the largest timestep that satisfies the CFL condition is chosen for computational efficiency.

B. Mesostructures

Provided below are example images of all mesostructures with voids from Table 2. Each example image is 200 µm by 25 µm (Figs. B.1 and B.2).

C. Validation data

Tables are provided with all regression rate data used in analysis and plotting (Tables C.1 and C.2). The mean, 95% upper, and 95% lower burn rates were found after omitting the first and last five saved timesteps due to transient effects from the laser initial condition and thermal boundary effects at the inlet and outlet. The error is calculated with,

$$\text{Error} = \frac{\text{(Comp. Burn Rate)-(Exp. Burn Rate)}}{\text{Exp. Burn Rate}}, \quad (1)$$

and then multiplied by 100 to convert to a percentage. The mean computational burn rate is used for all error calculations.

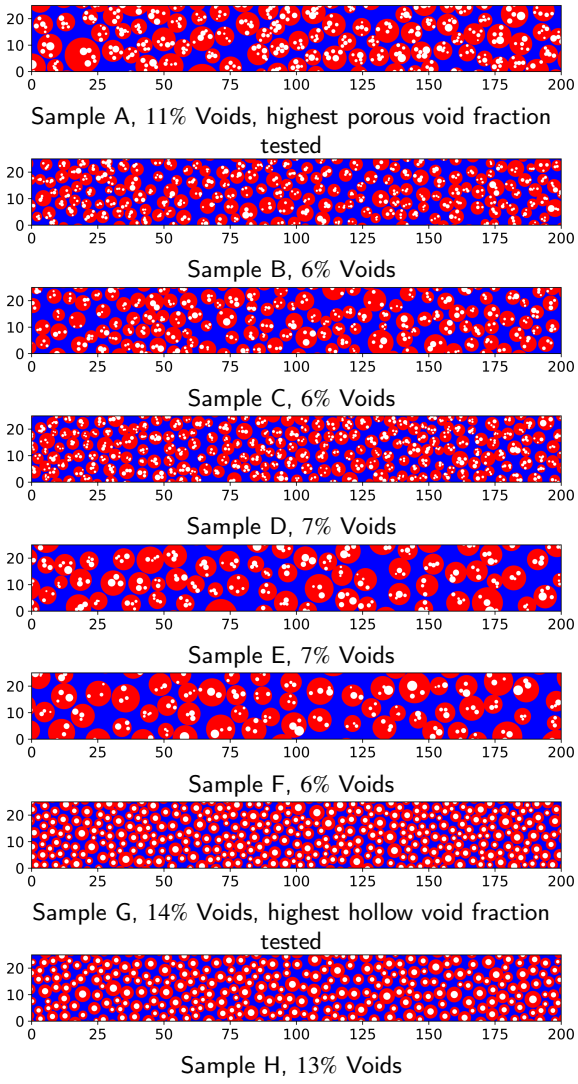

Figure B.1: Example images of mesostructures with voids. All mesostructures are 200 µm by 25 µm

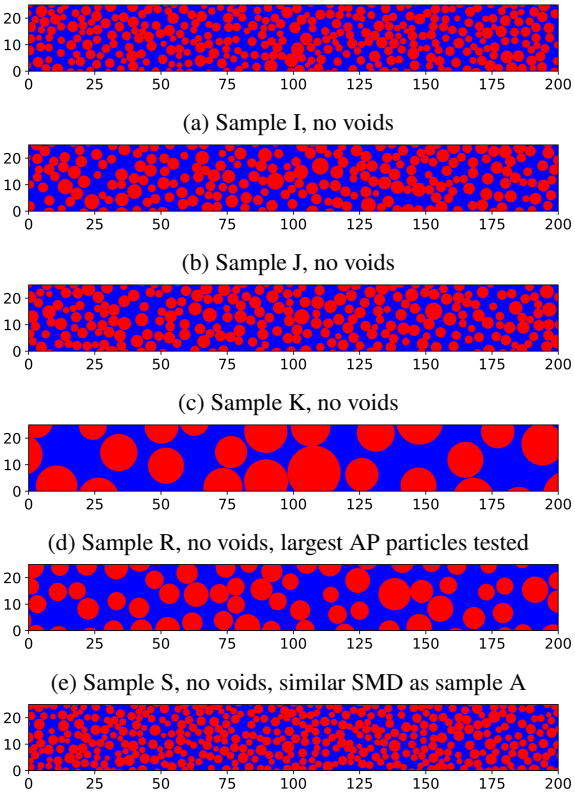

(a) Sample I, no voids

(b) Sample J, no voids

(c) Sample K, no voids

(d) Sample R, no voids, largest AP particles tested

(e) Sample S, no voids, similar SMD as sample A

(f) Sample T, no voids, smallest AP particles tested

Figure B.2: Example images of mesostructures without voids. All mesostructures are 200 µm by 25 µm

Table C.1
Burn rate (mm/s) comparison of model with experimental data at 1 MPa gauge pressure. The highest error is −27.89% in sample A

Sample	Burn Rate [mm/s]		Error %	95% Bound	
	Exp. [15]	Comp.	(−)	Upper	Lower
A	3.8	2.74	-27.89	3.81	1.46
B	3.2	2.92	-6.88	3.92	1.99
C	3.6	3.21	-10.83	4.15	2.23
D	3.2	2.65	-21.56	3.21	1.82
E	3.5	3.37	-3.71	4.54	1.76
F	3.0	3.59	19.67	5.78	1.76
G	4.6	5.67	23.26	6.56	4.85
H	5.1	6.23	22.16	6.81	5.58
I	3.4	3.75	10.29	4.79	3.12
J	3.2	3.37	5.31	4.57	2.19
K	3.2	3.37	5.31	4.78	2.45
R	2.2	1.71	-22.27	3.44	0.16
S	2.6	2.21	-15.00	4.79	0.62
T	3.5	3.67	13.43	4.84	3.32

Table C.2
Burn rate (mm/s) comparison of model with experimental data at 7 MPa gauge pressure. The highest error is 58.44% in sample F

Sample	Burn Rate (mm/s)		Error %	95% Bound	
	Exp. [15]	Comp	(−)	Upper	Lower
A	10.1	9.51	-5.84	10.74	7.99
B	7.1	10.15	42.96	10.57	9.52
C	7.6	10.28	35.26	10.80	9.77
D	7.2	9.35	29.86	9.77	8.97
E	7.8	9.95	27.56	10.88	9.08
F	6.4	10.14	58.44	11.35	8.71
G	13.1	9.44	-27.94	9.77	9.16
H	12.0	10.07	-16.08	10.54	9.68
I	7.2	5.56	-22.78	6.43	4.09
J	6.8	5.23	-23.09	7.27	3.46
K	6.9	5.28	-23.48	7.17	3.53
R	5.3	4.37	-17.55	8.65	2.09
S	6.0	4.73	-21.17	7.11	2.02
T	7.2	5.14	-28.61	5.94	4.56